

STAR-FORMING SITES IC 446 AND IC 447: AN OUTCOME OF END-DOMINATED COLLAPSE OF MONOCEROS R1 FILAMENT

N. K. BHADARI^{1,2}, L. K. DEWANGAN¹, L. E. PIROGOV³, AND D. K. OJHA⁴

ABSTRACT

We present an analysis of multi-wavelength observations of Monoceros R1 (Mon R1) complex (at $d \sim 760$ pc). An elongated filament (length ~ 14 pc, mass $\sim 1465 M_{\odot}$) is investigated in the complex, which is the most prominent structure in the *Herschel* column density map. An analysis of the FUGIN $^{12}\text{CO}(1-0)$ and $^{13}\text{CO}(1-0)$ line data confirms the existence of the filament traced in a velocity range of $[-5, +1]$ km s⁻¹. The filament is found to host two previously known sites IC 446 and IC 447 at its opposite ends. A massive young stellar object (YSO) is embedded in IC 446, while IC 447 contains several massive B-type stars. The *Herschel* temperature map reveals the extended warm dust emission (at $T_d \sim 15-21$ K) toward both the ends of the filament. The *Spitzer* ratio map of $4.5 \mu\text{m}/3.6 \mu\text{m}$ emission suggests the presence of photo-dissociation regions and signature of outflow activity toward IC 446 and IC 447. Based on the photometric analysis of point-like sources, clusters of YSOs are traced mainly toward the filament ends. The filament is found to be thermally supercritical showing its tendency of fragmentation, which is further confirmed by the detection of a periodic oscillatory pattern (having a period of $\sim 3-4$ pc) in the velocity profile of ^{13}CO . Our outcomes suggest that the fragments distributed toward the filament ends have rapidly collapsed, and had formed the known star-forming sites. Overall, the elongated filament in Mon R1 is a promising sample of the “end-dominated collapse” scenario, as discussed by Pon et al. (2011, 2012).

Subject headings: dust, extinction – III regions – ISM: clouds – ISM: individual object (Monoceros R1) – stars: formation – stars: pre-main sequence

1. INTRODUCTION

After the launch of the *Herschel* Space Observatory (Pilbratt 2010), filamentary structures have been commonly found in star-forming regions (e.g., André et al. 2010, 2014). Filaments having various physical scales, spanning from the scale of the molecular cloud to the scale of protostellar envelope (i.e., $\sim 100-0.1$ pc), have been reported in the literature (e.g., Myers 2009; Tobin et al. 2010; Hacar & Tafalla 2011; Goodman et al. 2014; Lu et al. 2018), and are often found to nurture star formation activities along their major axis (e.g., André et al. 2010; Schneider et al. 2012; Contreras et al. 2016; Dewangan et al. 2017c). The observational and theoretical studies suggest that filamentary clouds break into fragments of dense clumps and cores, which can further collapse to form young stellar objects (YSOs) as well as massive stars ($> 8 M_{\odot}$) (e.g., Bally et al. 1987; Bastien 1983, 1991; Heitsch et al. 2008; Myers 2009; Pon et al. 2011, 2012; Contreras et al. 2013; Clarke & Whitworth 2015; Kainulainen et al. 2016; Dewangan et al. 2017c, 2019). Massive fragments along the filaments have also been observed, where signatures of potential massive protostars are found (e.g., Jackson et al. 2010; Schneider et al. 2010; Busquet et al. 2013; Beuther et al. 2015; Dewangan et al. 2019, and references therein). Previous

studies suggest that filaments can magnify the infall accretion rates to individual clumps, and thus can form massive stars (Banerjee & Pudritz 2008; Myers 2009). Hence, the role of filaments in star formation has been evident. However, the physical processes that govern the filamentary fragmentation and the formation of massive clumps/cores and clusters of YSOs are still debatable (e.g., Myers 2009; Schneider et al. 2012; André et al. 2014; Baug et al. 2015; Contreras et al. 2016; Dewangan et al. 2015, 2016a,b, 2017a,b,c,d,e, 2019).

Analytical studies of the infinitely long, hydrostatic cylindrical clouds suggest that filaments are gravitationally unstable to axisymmetric perturbations resulting in the fragmentation at equal spacing (e.g., Inutsuka & Miyama 1992, 1997; Nakamura et al. 1993). In the case of long but finite-sized filaments, the local collapse time-scale is observed as a function of relative axial position, and the collapse occurs faster at the ends of the filament compared to its central part (i.e., end-dominated collapse; Bastien 1983; Pon et al. 2011, 2012). However, observational evidences of numerical studies, in particular “end-dominated collapse”, are a few in the literature (e.g., Zernickel et al. 2013; Beuther et al. 2015; Hacar et al. 2016; Kainulainen et al. 2016; Dewangan et al. 2017c, 2019; Yu et al. 2019). In this context, to observationally assess the existing numerical simulations concerning star-forming filaments, we have selected a nearby star-forming site in Monoceros R1 (hereafter Mon R1) complex using a multi-scale and multi-wavelength approach.

Mon R1 is a clustering of reflection nebulae (i.e., R-association), located toward the Galactic plane and allied with the well-studied OB association Mon OB1 (van den Bergh 1966). It is situated about 2° away from the centre of Mon OB1 (i.e., Cone Nebula NGC 2264; see

naval@prl.res.in

¹ Physical Research Laboratory, Navrangpura, Ahmedabad - 380 009, India.² Indian Institute of Technology Gandhinagar Palaj, Gandhinagar - 382355, India.³ Institute of Applied Physics of the Russian Academy of Sciences, 46 Ulyanov st., Nizhny Novgorod 603950, Russia.⁴ Department of Astronomy and Astrophysics, Tata Institute of Fundamental Research, Homi Bhabha Road, Mumbai 400 005, India.

an inverted C-like structure of Mon R1 association (coordinates \sim RA: $6^{\text{h}} 31^{\text{m}} 0^{\text{s}}$, Dec: $+10^{\circ} 00' 00''$) in Figure 1 of Montillaud et al. 2019). Several distances (e.g., 715 pc (van den Bergh 1966), 800 pc (Stahler & Palla 2005), 900 pc (Oliver et al. 1996), 1000 pc (Kutner et al. 1979)) to Mon R1 are reported in the literature. In this paper, we adopt a heliocentric distance of ~ 760 pc for Mon R1 (e.g., Montillaud et al. 2019). The reflection nebulae NGC 2245, NGC 2247, IC 446, IC 447 and, several early type (B3–B7) stars including VdB 76, VdB 77, VdB 78, are members of the Mon R1 association (Kutner et al. 1979). Figure 1a displays the *Planck* sub-millimeter image at $550 \mu\text{m}$ of R-association, where the locations of NGC 2245, NGC 2247, IC 446, and IC 447 are marked. The direction in the figure is presented in the Galactic coordinates. In Figure 1b, we show a false-color optical image at Digitized Sky Survey II (hereafter DSS2) $0.47 \mu\text{m}$ (size $\sim 1^{\circ}.04 \times 0^{\circ}.89$ or corresponding physical extent $\sim 13.8 \text{ pc} \times 11.8 \text{ pc}$ at $d \sim 760 \text{ pc}$). The locations of reflection nebulae along with the previously known bright OB-type stars are also highlighted, and are listed in Table 1. In the optical image, one can clearly see that two sites IC 446 and IC 447 are connected by a curved section of dark nebulosity, which is indicated by arrows in Figure 1b. This dark nebulosity appears bright in the *Planck* image at $550 \mu\text{m}$, and can be referred to as an elongated filamentary structure. In other words, the sites IC 446 (or IC 2167) and IC 447 (or IC 2169) are seen at opposite ends of the filamentary structure. A massive YSO, VY Mon is also reported toward the site IC 446 (e.g., Casey & Harper 1990).

Using the molecular CO line observations (resolution $\sim 1'.1\text{--}2'.6$), Kutner et al. (1979) studied the molecular gas toward R-association and Mon OB1. The Mon R1 molecular cloud, traced in a radial velocity (V_{lsr}) range of $[-1, 5] \text{ km s}^{-1}$, was found to be kinematically distinct from the Mon OB1 molecular complex at $[5, 10] \text{ km s}^{-1}$. A partial ring structure of the Mon R1 molecular cloud was observed in the molecular map at $[-1, 5] \text{ km s}^{-1}$, which hosts the above mentioned reflection nebulae in its periphery. The *Planck* continuum image at $550 \mu\text{m}$ also shows a semi-ring structure in Figure 1a. However, Kutner et al. (1979) found at least two velocity components toward Mon R1 at $[-1, 1]$ and $[3, 5] \text{ km s}^{-1}$ (see Figure 2 in Kutner et al. 1979). The cloud at $[3, 5] \text{ km s}^{-1}$ was associated with NGC 2245 and NGC 2247, while a semi-circular arc of cloud hosting the sites IC 446 and IC 447 was reported in a velocity range of $[-1, 1] \text{ km s}^{-1}$ (see Figure 2 in Kutner et al. 1979). The elongated morphology of the cloud component at $[-1, 1] \text{ km s}^{-1}$ is also observed in other wavelengths; thus we prefer to categorize it as a filament. Kutner et al. (1979) proposed that a previous energetic event, such as expanding H II regions, stellar winds, or SN blast waves, was responsible for the existence of the partial ring structure in the Mon R1 molecular cloud at $[-1, 5] \text{ km s}^{-1}$. They also pointed out that the physical process, which governs the formation of observed OB-stars toward the region, might be different. In this connection, we observationally try to resolve the ambiguity of physical process governing the star formation activity toward the filamentary cloud at $[-1, 1] \text{ km s}^{-1}$. To understand the physical mechanism(s) of star formation in Mon R1 cloud, we have examined the dis-

tribution of molecular gas, ionized emission, dust (i.e., warm and cold) emission, and YSOs.

Based on the previous studies, we find that Mon R1 is a relatively nearby star-forming complex hosting the elongated filamentary structure as well as massive B-type stars, making Mon R1 as an important target site for probing star formation processes. The *Herschel* temperature and column density maps (resolution $\sim 12''$) are utilized to study the distribution of dust temperature and column density, while high resolution FOREST Unbiased Galactic plane Imaging survey with the Nobeyama 45-m telescope (FUGIN; Umemoto et al. 2017) molecular line data (resolution $\sim 20''$) are employed to examine the gas flow toward the Mon R1 molecular cloud. Furthermore, the observational findings derived in this work have been used to assess the existing theoretical models related to star-forming filaments.

Following the introduction in this section, we present the adopted data sets in Section 2. The observational outcomes are presented in Section 3. In Section 4, we discuss our observational results against the existing theoretical models. Finally, Section 5 gives the main conclusions of this paper.

2. DATA AND ANALYSIS

Figure 1a displays the target area (central coordinates $l = 201^{\circ}.5$, $b = 0^{\circ}.5$) of the present study. The selected target area has an angular extent of $\sim 1^{\circ}.5 \times 1^{\circ}.4$, which corresponds to a physical scale of $\sim 20.3 \text{ pc} \times 18.1 \text{ pc}$ (at $d \sim 760 \text{ pc}$). Various publicly available multi-wavelength and multi-scale data-sets have been explored in this paper, which are listed in Table 2. In the direction of our selected target area, we retrieved $^{12}\text{CO}(J=1-0)$ and $^{13}\text{CO}(J=1-0)$ line data from the FUGIN survey, which are calibrated in main beam temperature (T_{mb} , see Umemoto et al. 2017). The typical RMS noise level¹ (T_{mb}) is $\sim 1.5 \text{ K}$ and $\sim 0.7 \text{ K}$ for ^{12}CO and ^{13}CO lines, respectively (Umemoto et al. 2017). The FUGIN survey provides the data with a velocity resolution of 1.3 km s^{-1} . In order to improve sensitivities, we have smoothed each FUGIN molecular line data cube with a Gaussian function having half-power beamwidth of 3 pixels.

The *Herschel* temperature and column density ($N(\text{H}_2)$) maps (resolution $\sim 12''$) were obtained from a publicly accessed website², and were generated for the *EU-funded ViaLactea project* (Molinari et al. 2010b). To produce these maps, the Bayesian algorithm, *Point Process Mapping* (PPMAP) method (Marsh et al. 2015, 2017), was applied on the *Herschel* images at 70, 160, 250, 350, and $500 \mu\text{m}$.

3. RESULTS

3.1. *Herschel* column density and temperature maps

Figures 1a and 1b have enabled us to infer the existence of the elongated filamentary structure. In order to further examine the filament, in Figures 2a and 2b, we display the *Herschel* temperature and column density ($N(\text{H}_2)$) maps of the target region (see a dashed cyan box in Figure 1a), respectively. The *Herschel* temperature map shows the extended warm dust emission

¹ <https://nro-fugin.github.io/status/>

² <http://www.astro.cardiff.ac.uk/research/ViaLactea/>

Table 1

List of bright stars known toward Mon R1 complex (see Figure 1b). The positions and spectral type of stars are given in the table.

ID	Name	l (degree)	b (degree)	Spectral-type	Association	References
1	TYC 737-255-1	201.32	+00.30	B2.5V D	IC 446	–
2	VY Mon	201.34	+00.29	A5 Vep	IC 446	Mora et al. (2001)
3	V727 Mon	201.79	+00.07	B8V D	IC 447	–
4	VdB 76	201.63	+00.05	B7IIIp	IC 447	Racine (1968)
5	VdB 77	201.88	−00.03	B5III D	IC 447	Racine (1968)
6	VdB 78	201.93	+00.02	B3 E	IC 447	Cannon & Pickering (1993)
7	BD+09 1264	201.82	−00.09	OB E	IC 447	Nassau et al. (1965)
8	V699 Mon	201.77	+00.51	B7IIne C	NGC 2245	Herbst et al. (1982)
9	VdB 82	201.67	+00.67	B6ep D	NGC 2247	Herbst et al. (1982)

Table 2

List of multi-wavelength surveys used in this paper.

Survey	band(s)	Resolution	Reference
NRAO VLA Sky Survey (NVSS)	21 cm	$\sim 45''$	Condon et al. (1998)
FUGIN survey	$^{12}\text{CO}(J=1-0), ^{13}\text{CO}(J=1-0)$	$\sim 20'', \sim 21''$	Umemoto et al. (2017)
Planck Survey	$550 \mu\text{m}$	$4'.8$	Planck Collaboration IX (2014)
Herschel Infrared Galactic Plane Survey (Hi-GAL)	70, 160, 250, 350, 500 μm	$5''.8, 12'', 18'', 25'', 37''$	Molinari et al. (2010a)
Wide Field Infrared Survey Explorer (WISE)	$22 \mu\text{m}$	$\sim 12''$	Wright et al. (2010)
Warm-Spitzer GLIMPSE360 Survey	3.6, 4.5 μm	$\sim 2''$	Benjamin et al. (2003)
UKIRT near-infrared Galactic Plane Survey (GPS)	1.25–2.2 μm	$\sim 0''.8$	Lawrence et al. (2007)
Two Micron All Sky Survey (2MASS)	1.25–2.2 μm	$\sim 2''.5$	Skrutskie et al. (2006)
Digitized Sky Survey II (DSS2)	0.47 μm	$\sim 2''$	McLean et al. (2000)

(at $T_d \sim 15\text{--}21$ K) toward the sites IC 446, IC 447, and NGC 2245. The elongated filament is revealed as the most prominent feature in the *Herschel* column density map and is traced using the $N(\text{H}_2)$ contour level of $3.2 \times 10^{21} \text{ cm}^{-2}$. It is not a straight filament, but shows a curved geometry. The column density map also exhibits the presence of several high column density (i.e., $6\text{--}9 \times 10^{21} \text{ cm}^{-2}$) regions toward the filament. The boundary of the elongated filament (length ~ 14 pc) is shown in Figure 3a and is identified using the IDL *clumpfind* algorithm (Williams & Blitz 1994). The *clumpfind* algorithm decomposes 2- and 3-dimensional data into disjoint clumps of emission. The algorithm requires contouring of data with a multiple of RMS noise and then finds positions of peak emission which correspond to the clumps, and further follows them down to the lower intensities (Williams & Blitz 1994). In other words, one needs the lowest contour level, below which data is rejected, and the interval between contours as input parameters for the *clumpfind* algorithm.

Considering the curved morphology of the filament, it can be divided into three parts, which are referred to as eastern, central, and western parts. The eastern one, toward the site IC 447, is more diffuse with a single column density peak, while the central part (length ~ 5 pc) and the western one toward the site IC 446 (length $\sim 2\text{--}4$ pc) are more dense and have several column density peaks. In the direction of the elongated filament, Figure 3b displays the boundaries of two sub-filaments identified using the IDL *clumpfind* algorithm. Here, the $N(\text{H}_2)$ contour level of $4.1 \times 10^{21} \text{ cm}^{-2}$ was used as an input for the *clumpfind* algorithm. These sub-filaments are seen toward the central and western parts of the elongated filament as highlighted in Figure 3a. These sub-filaments appear linear, but are not colinear to each other.

To calculate the total mass of the elongated filament

(length ~ 14 pc) and sub-filaments, we use the following relation as given in Dewangan et al. (2017c)

$$M_{\text{clump}} = \mu_{\text{H}_2} m_{\text{H}} a_{\text{pixel}} \Sigma N(\text{H}_2) \quad (1)$$

where, μ_{H_2} is the mean molecular mass (assumed to be 2.8), a_{pixel} is the area subtended by one pixel, m_{H} is the mass of hydrogen atom, and $\Sigma N(\text{H}_2)$ is the integrated column density over the area of the clump. We have computed the total mass of the elongated filament (M_{filament}) to be $\sim 1465 M_{\odot}$. The total mass of the central and western parts of the filament is determined to be ~ 319 and $\sim 365 M_{\odot}$, respectively. The importance of these results is discussed in Section 4.2.

In general, the observed line mass of a filament can be calculated as the ratio of M_{filament} to its length. In this work, adopting the values of $M_{\text{filament}} \sim 1465 M_{\odot}$ and length ~ 14 pc, the observed line mass of the filament is determined to be $M_{\text{l,obs}} \sim 105 M_{\odot} \text{ pc}^{-1}$. Length of the filament is measured along its major axis with the use of DS9 software³. The line mass of the filament depends upon the “cos i ” factor (e.g., Kainulainen et al. 2016), where “ i ” is the angle between the filament’s major axis and the sky plane. Since we do not have the information of “ i ”, we assume that the filament lies to the same plane as that of the sky plane. Hence, the value of the inclination angle can be taken as zero (i.e., $i = 0$), yielding the value of $\cos i = 1$. Therefore, the observed line mass per unit length can be assumed as an upper limit (e.g., Kainulainen et al. 2016). Additionally, the total mass of the filament ($M_{\text{filament}} \sim 1465 M_{\odot}$) can be underestimated because its small portion (FoV $\sim 8'\text{--}14'$) is unavailable in the *Herschel* column density map at higher latitude (for comparison, see Figures 3a and 5c). It is clear from Eq. 1, the uncertainty in the mass of filament varies lin-

³ <http://hea-www.harvard.edu/RD/ds9/>

early with the $N(\text{H}_2)$ uncertainties.

3.2. Infrared and Radio view of R-association

Figure 4a presents the mid-infrared (MIR) image at WISE 22 μm of the R-association, which may trace the warm dust emission in our selected target area. The WISE image is overlaid with the NVSS 1.4 GHz continuum emission contours (beam size $\sim 45''$; $1\sigma \sim 0.45$ mJy beam $^{-1}$; Condon et al. 1998). No extended HII region is found in our selected target area. However, several massive stars have been reported toward the sites IC 447 and IC 446 (see Figure 1b and also Table 1), where extended warm dust emission is observed.

We have also carefully examined the *Spitzer* 3.6 and 4.5 μm continuum images to explore the physical environment in Mon R1. In Figure 4b, we display the *Spitzer* ratio map of 4.5 $\mu\text{m}/3.6 \mu\text{m}$ emission, which shows bright and dark regions depicting the dominance of 4.5 μm flux over the 3.6 μm flux and vice versa. It is known that these two *Spitzer* images have the same point spread function (PSF). Hence, one can produce the *Spitzer* ratio map of 4.5 $\mu\text{m}/3.6 \mu\text{m}$ emission, which allows us to remove point-like sources as well as continuum emission (e.g., Dewangan et al. 2017a). The *Spitzer* band at 3.6 μm contains polycyclic aromatic hydrocarbon (PAH) emission at 3.3 μm , while the molecular hydrogen line ($\nu = 0-0$ S(9); 4.693 μm) and the Br- α emission (at 4.05 μm) are covered in the *Spitzer* band at 4.5 μm . In the ratio map, the bright emission is found toward IC 446, where no NVSS continuum emission (or ionized emission) is detected. Hence, the area with bright emission toward IC 446 may be associated with the outflow activity (see also Section 3.4). Furthermore, in the ratio map, the dark or grey regions toward IC 447 display the dominance of 3.3 μm PAH feature, indicating the presence of photodissociation regions (PDRs; see Tielens 2008). It also favours the impact of massive stars toward IC 447.

3.3. Kinematics from spectral line data

In this section, we present the results derived using the analysis of the FUGIN $^{12}\text{CO}(J=1-0)$ and $^{13}\text{CO}(J=1-0)$ line data.

3.3.1. Integrated molecular maps

In this section, using the FUGIN $^{12}\text{CO}(J=1-0)$ and $^{13}\text{CO}(J=1-0)$ line data, we present kinematic properties of the molecular cloud(s) associated with our selected target area (see a broken yellow box in Figure 1a). Figures 5a–5f display the CO maps of intensity (moment-0) in the direction of Mon R1. In Figures 5a and 5b, the ^{12}CO and ^{13}CO emissions are integrated over a velocity range of $[-7.8, 10.4]$ km s $^{-1}$, respectively. The molecular maps at $[-7.8, 10.4]$ km s $^{-1}$ show the gas toward NGC 2245, NGC 2247, and the filament containing the sites IC 446 and IC 447. Figures 5c and 5d present the ^{12}CO and ^{13}CO maps integrated over a velocity range of $[-7.8, 1.3]$ km s $^{-1}$, respectively. In these maps, the molecular emission is observed mainly toward the filament containing the sites IC 446 and IC 447. In Figures 5e and 5f, the ^{12}CO and ^{13}CO emissions are integrated over a velocity range of $[1.95, 10.4]$ km s $^{-1}$, respectively. The molecular maps at $[1.95, 10.4]$ km s $^{-1}$ display the molecular emission toward the sites NGC 2245 and

NGC 2247. As mentioned in the Introduction section, the previous study of the Mon R1 clouds (Kutner et al. 1979) suggested the presence of two distinct clouds in the velocity range of $[-1, 1]$ and $[3, 5]$ km s $^{-1}$. However, our analysis is benefited with the availability of high resolution molecular line data compared to the previous study (e.g., Kutner et al. 1979). In this paper, the analysis of the FUGIN line data also favours the existence of two distinct molecular clouds in the direction of Mon R1 as discussed by Kutner et al. (1979).

To study the gas flow in the filament, we have selected an area (see a broken box in Figure 5; extension $\sim 0^\circ.99 \times 0^\circ.71$ or ~ 13.14 pc \times 9.42 pc at $d \sim 760$ pc) toward the target region. In Figures 6a and 6b, the channel maps of ^{12}CO and ^{13}CO are presented in a velocity range of $[-7.8, 1.95]$ km s $^{-1}$, respectively. To examine the gas flow in the direction of the filament, we have overlaid the *Herschel* 160 μm continuum emission contour to highlight the extent of the filament. The molecular emission is prominently seen in the velocity range of $[-2.6, -0.65]$ km s $^{-1}$, allowing to trace the boundary of the filament. However, in the channel maps of ^{12}CO and ^{13}CO , the gas flow toward the filament is observed in a velocity range of $[-5, +1]$ km s $^{-1}$.

3.3.2. Position Velocity ($p-v$) diagrams

The presence of two clouds is further examined by the analysis of the position-velocity ($p-v$) diagrams of molecular gas. Figures 7a and 7c present the latitude-velocity ($b-v$) diagrams of ^{12}CO and ^{13}CO toward the field of view as shown in Figure 5, respectively. In order to extract the $b-v$ diagrams, the molecular emission is integrated over the longitude range from 201° to 202° . In Figures 7b and 7d, we show the longitude-velocity ($l-v$) diagrams of ^{12}CO and ^{13}CO , respectively. To obtain the $l-v$ diagrams, the molecular emission is integrated over the latitude range from $-0^\circ.16$ to $0^\circ.45$.

All the position-velocity diagrams show two velocity components toward Mon R1, which do not seem to be connected in velocity space. Hence, we find that the molecular gas toward the filament is traced mainly in a velocity range of $[-5, +1]$ km s $^{-1}$ (see a dashed rectangular box in Figure 7). These exercises also allow us to infer the exact boundary of the filamentary cloud, suggesting the existence of a single and isolated filament in Mon R1 (see also Figure 6).

3.3.3. Velocity field of the gas

Figure 8a shows the integrated intensity (or moment-0) map of ^{13}CO , where 31 distinct positions toward the filament are highlighted by filled blue circles (radius $\sim 10''$ each). In order to examine the velocity variation of the gas toward the filament, we have extracted the averaged spectra toward each circle marked in Figure 8a. These positions are chosen where the ^{13}CO integrated intensities are locally maximum than their surroundings. The observed spectra were then fitted with the Gaussian profile(s), and the spectral parameters (e.g., radial velocity (V_{lsr}) and linewidth (ΔV)) are derived. The velocity profile (i.e., velocity vs length along major axis) of the filament is shown in Figure 8b, which suggests that the filament has a maximum velocity variation of ~ 3 km s $^{-1}$. The velocity profile also shows an oscillatory pattern

(with a period of $\sim 3\text{--}4$ pc), which becomes more prominent when we remove the linear gradient from the profile. There are two prominent velocity peaks separated by $\sim 8\text{--}9$ pc (see Figures 8b and 8c), which are associated with the central and western parts of the filament. The negative and positive velocity gradients between these peaks could be connected with different inclinations of the different parts of the filament. The velocity profile after removing the linear gradient is shown in Figure 8c. There is a clear linear velocity gradient along the central part of the filament ($\sim 0.4 \text{ km s}^{-1} \text{ pc}^{-1}$) and also velocity gradients ($\sim 0.6 \text{ km s}^{-1} \text{ pc}^{-1}$) at the ends, which are probably associated with star-forming regions. The linewidth (ΔV) profile is shown in Figure 8d, where one can obtain the average linewidth to be $\sim 1.5 \text{ km s}^{-1}$. The significance of these results concerning the filamentary fragmentation is discussed in Section 4.

3.4. Distribution of young stellar objects

In a given star-forming region, star formation activity is often traced by the distribution of YSOs. The population of YSOs toward the R-association is identified using the color-color and color-magnitude diagrams (see Figures 9a and 9b). Figure 9a shows the dereddened color-color diagram (i.e., $[[3.6] - [4.5]]_0$ vs $[K - [3.6]]_0$) of point-like objects extracted from the Warm-*Spitzer* Glimpse360⁴ (Whitney et al. 2011) survey. In the dereddened color-color diagram, triangles and circles represent Class I and Class II YSOs, respectively. Following the conditions given in Gutermuth et al. (2009), we identified a total of 201 YSOs (i.e., 8 Class I and 193 Class II YSOs) in our selected target area.

Additional sources with color-excess emission are also obtained from the examination of the NIR color-magnitude ($H - K$ vs K) diagram (see Figure 9b). Here we obtained the photometric data from the 2MASS and UKIDSS-GPS surveys. In order to obtain the credible photometric magnitudes of point-like sources from the 2MASS and UKIDSS-GPS surveys, we selected those sources which have photometric uncertainties of $\sigma < 0.1$ mag in H and K bands (see also Dewangan et al. 2017a, for more details). Following a color condition of $H - K > 1$ mag, we obtain a total of 182 YSO candidates in our selected area (see blue squares in Figure 9b). This color condition is decided based on the color-magnitude analysis of a nearby control field.

Altogether, a total sum of 370 YSO candidates is selected after counting the common YSOs traced in Figures 9a and 9b. In Figure 9c, the positions of these selected YSOs are overlaid on the *Herschel* 160 μm continuum image of Mon R1. We have overplotted the *Herschel* 160 μm continuum emission contour to indicate the location of the filament. In order to study the concentration of YSOs in our selected area, we have carried out the nearest neighbor (NN) surface density analysis of all the selected YSOs (see e.g., Casertano & Hut 1985; Gutermuth et al. 2009; Bressert et al. 2010; Dewangan et al. 2017a). Adopting similar procedures as highlighted in Dewangan et al. (2017a), the surface density map of YSOs has been generated using a $15''$ grid and 6 NN at a distance of 760 pc.

In Figure 9d, we overlay the surface density contours (in cyan) of YSOs on the *Herschel* 160 μm image. The surface density contours of YSOs are shown with the levels of 4, 5, 8, 10, 20, 35, 55, and 125 YSOs pc^{-2} , tracing the zones of star formation in our selected site. The YSOs are clustered mainly toward the ends of the filament (i.e., IC 446 and IC 447). In the direction of IC 446, we find higher surface density of YSOs (i.e., 4–125 YSOs pc^{-2}), while the surface density values are found to be 4–12 YSOs pc^{-2} toward IC 447. This particular analysis suggests that star formation activity is more intense toward IC 446 compared to IC 447 in the filament. It is also noted that the site IC 447 hosts several evolved massive B-type stars.

Most recent narrow-band $H\alpha$ and $[S\text{II}]$ imaging observations of Mon R1 region (including sites NGC 2245, NGC 2247, and IC 446) by Movsessian et al. (2020, submitted to MNRAS) show the presence of at least 4 Herbig-Haro (HH) objects toward the filament (see Figures 2 and 4 in their paper). Three out of them (i.e., HH 1202A, HH 1202B, and HH 1202C) are observed toward the site IC 446, while the remaining fourth one (i.e., HH 1203) is seen near the junction of the central and western parts of the filament. The detection of HH objects also favours high activity of star formation in the filament.

4. DISCUSSION

The presence of a filament itself represents first step toward the formation of embedded cores and stars. However, second and major step is gravitational fragmentation which leads to the fabrication of self-gravitating cores (André et al. 2010, 2014). In this context, our observational results can be compared with the existing theoretical models of filamentary fragmentation and collapse.

4.1. Mon R1 filament: a supercritical filament

In the literature, gravitational instability of a filament is defined by its critical line mass parameter. One can calculate the critical line mass of a filament ($M_{1,\text{cri}}$) by considering it as an infinite and non-magnetized isothermal cylinder, which is in equilibrium between gravitational and thermal pressures. $M_{1,\text{cri}}$ is a function of the kinetic temperature (T_k) of the gas only, and can be expressed as follows (Ostriker 1964):

$$M_{1,\text{cri}} = \frac{2c_s^2}{G} \simeq \frac{16M_\odot}{pc} \left(\frac{T_k}{10\text{K}} \right) \quad (2)$$

where $c_s = \sqrt{\frac{kT_k}{\mu m_H}}$ is the isothermal speed of sound at T_k , and G is the universal gravitational constant. Considering $T_k = 10$ K and the mean molecular weight $\mu = 2.33$, the value of c_s comes out to be $\sim 0.19 \text{ km s}^{-1}$. Thus, $M_{1,\text{cri}}$ is estimated to be $\sim 24\text{--}32 M_\odot \text{ pc}^{-1}$ for a temperature range of 15–20 K. In this work, the value of $M_{1,\text{obs}}$ is determined to be $\sim 105 M_\odot \text{ pc}^{-1}$ (see Section 3.1), which greatly exceeds the value of $M_{1,\text{cri}}$.

Inutsuka & Miyama (1992) found that the isothermal filaments with $M_{1,\text{obs}} > M_{1,\text{cri}}$ become unstable to axisymmetric perturbation and collapse radially toward their axis. Such filaments are classified as thermally *supercritical*, which often found to nurture the prestellar

⁴ <http://www.astro.wisc.edu/sirtf/glimpse360/>

cores and embedded YSOs (e.g., André et al. 2010; Dewangan et al. 2017c). However, the isothermal filaments which follow the condition $M_{1,\text{obs}} < M_{1,\text{cri}}$ are designated as *subcritical* filaments, and show the deficiency of star formation activity (e.g., André et al. 2010; Dewangan et al. 2017c). Following the above statements, Mon R1 filament is found to be thermally *supercritical* in nature. The presence of the *Herschel* clumps/sub-filaments and groups of YSOs toward the thermally *supercritical* filament in Mon R1 suggests that it is more prone to fragment and able to collapse into cores due to gravitational instability (André et al. 2010).

There is a possibility that the non-thermal microturbulent gas motions can provide extra support to the filament against gravitational collapse as these motions are associated with the gas turbulence (e.g., Hacar & Tafalla 2011). This additional support increases the $M_{1,\text{cri}}$ of the filament. The new line mass is termed as virial line mass ($M_{1,\text{vir}}$) and can be estimated by replacing c_s with the effective sound speed i.e., $c_{s,\text{eff}} = \sqrt{c_s^2 + \sigma_{\text{NT}}^2}$ in Eq. 2 (e.g., Kainulainen et al. 2016; Dewangan et al. 2019). In the expression of $c_{s,\text{eff}}$, σ_{NT} represents the non-thermal velocity dispersion that can be expressed as (e.g., Dewangan et al. 2018)

$$\sigma_{\text{NT}} = \sqrt{\frac{\Delta V^2}{8 \ln 2} - \frac{kT_k}{29m_H}} = \sqrt{\frac{\Delta V^2}{8 \ln 2} - \sigma_{\text{T}}^2} \quad (3)$$

where ΔV is the observed linewidth of ^{13}CO spectra, and $\sigma_{\text{T}} = \sqrt{\frac{kT_k}{29m_H}}$ is the thermal broadening for ^{13}CO at the gas kinetic temperature (T_k).

In this work, the linewidth of ^{13}CO spectra is observed to be $\sim 1.5 \text{ km s}^{-1}$ (see Figure 8d), which leads the value of $M_{1,\text{vir}} \sim 211\text{--}219 M_{\odot} \text{ pc}^{-1}$ for a temperature range of $\sim 15\text{--}20 \text{ K}$. The values of $M_{1,\text{vir}}$ and $M_{1,\text{obs}}$ are close to each other within a factor of ~ 2 . Mach number, defined as the ratio of σ_{NT}/c_s , is determined in a range of 2.4–2.7 for the filament, which suggests the supersonic nature of the filament.

4.2. Age Estimates

Several high column density regions (i.e., fragments) are evident in the *Herschel* column density map, indicating the fragmentation of Mon R1 filament (e.g., Kainulainen et al. 2016). Due to the curved morphology, the elongated filament is divided into three parts (see Section 3.1), which can also be traced in the molecular maps of CO (see Figures 5c and 5d). The eastern part containing the site IC 447 shows a separate filamentary branch in CO, while the central and western parts show linear geometries. Considering length of the central sub-filament (i.e., $\sim 5 \text{ pc}$) and the western sub-filament (i.e., $\sim 4 \text{ pc}$), the value of $M_{1,\text{obs}}$ is computed to be ~ 64 and $\sim 91 M_{\odot} \text{ pc}^{-1}$, respectively (see Section 3.1).

One can estimate a timescale at which a filament grows via accretion and reaches its $M_{1,\text{cri}}$ value. This timescale is referred to as critical timescale (τ_{cri}), which represents the lower age limit of the filament (Clarke et al. 2016). They showed that τ_{cri} is a function of fragmentation length scale (i.e., fragment/core separation, λ_{core}), which can be expressed as follows (Williams et al. 2018):

$$\tau_{\text{age}} \geq \tau_{\text{cri}} \simeq \frac{\lambda_{\text{core}}}{2c_s} \quad (4)$$

We have estimated λ_{core} along the central and western parts of Mon R1 filament, which is $\sim 0.5 \text{ pc}$ and $\sim 0.2 \text{ pc}$, respectively (see Figures 2b and 8c). For $c_s \sim 0.23 \text{ km s}^{-1}$ (at $T_k = 15 \text{ K}$), these core separation values lead τ_{cri} to be $\sim 1.1 \text{ Myr}$ and $\sim 0.4 \text{ Myr}$ for the central and western parts, respectively. The corresponding average accretion rate during the assembly of filament can also be calculated using $\dot{M} = \frac{M_{1,\text{cri}}}{\tau_{\text{cri}}}$ (e.g., Clarke et al. 2016; Williams et al. 2018). Thus, considering $M_{1,\text{cri}} \sim 24 M_{\odot} \text{ pc}^{-1}$ (at $T_k = 15 \text{ K}$) for both the central and western parts of the filament, the average accretion rate experienced during the growth of these parts of filament is ~ 22 and $\sim 60 M_{\odot} \text{ pc}^{-1} \text{ Myr}^{-1}$, respectively.

If we assume that the accretion rate remained constant over the filament's lifetime, then the age of the filament can be estimated using $\tau_{\text{age}} = \frac{M_{1,\text{obs}}}{\dot{M}}$ (e.g., Williams et al. 2018). This exercise yields the values of τ_{age} to be ~ 3 and $\sim 1.5 \text{ Myr}$ for the central and western parts of the filament, respectively. Therefore, the elapsed time since the central and western parts of the filament become critical, is ~ 1.9 and $\sim 1.1 \text{ Myr}$, respectively. However, considering the turbulence into account c_s can be replaced by $c_{s,\text{eff}}$ in Eq. 4. Adopting $T_k = 15 \text{ K}$ and $\Delta V \sim 1.5 \text{ km s}^{-1}$ (i.e., FWHM(^{13}CO)), the corresponding critical age for the central and western parts becomes ~ 0.4 and $\sim 0.2 \text{ Myr}$, respectively. The projection effects are not taken into account in the estimations of λ_{core} . Therefore, all these calculations give lower limits on the derived values of ages.

We use the ^{13}CO line data to trace the velocity profile of the filament. Figures 8b and 8c show an ordered oscillatory pattern in velocity (with a period of $\sim 3\text{--}4 \text{ pc}$) along the major axis of the filament. The previous study of L1517 dark cloud by Hacar & Tafalla (2011) showed a similar trend in the velocity profile. They also performed the fragmentation model for L1517 dark cloud and found that the velocity centroids peak at the locations of fragments, indicating gas motion associated with the fragments. Similar trends have also been observed in the other studies (e.g., Hacar et al. 2016; Kainulainen et al. 2016; Lu et al. 2018; Dewangan et al. 2019). These observational signatures of the fragmentation in filaments are also consistent in Mon R1 filament. However, to study the nature of fragments in Mon R1 filament, one requires detail modelling of filament using the information of so far unknown properties (i.e., orientation, geometry and strength of the magnetic field). Also, the availability of dense gas tracers in the filaments (e.g., HNC (1–0); Jackson et al. (2010), HCO⁺ (3–2); Zernickel et al. (2013), N₂H⁺ (1–0); Beuther et al. (2015), NH₃ (1–1, 2–2); Lu et al. (2018), CS (2–1); Dewangan et al. (2019)) can further constrain the velocity field which is the observational limitation of our current work.

4.3. Star Formation Scenario

Two different collapse modes of a filament have been discussed by Pon et al. (2012) in their study. They suggest that the interior of the filament collapses homogeneously, while its ends are preferentially given more mo-

mentum thus tend to collapse faster. In the case of the homologous collapse, density remains uniform and all the regions have a similar collapse timescale. The analytical study of an elongated but finite-sized filament suggests that the collapse timescale depends upon the relative position along the filament and it is shorter at the edges of the filament (Bastien 1983; Pon et al. 2011). For a filament having an initial aspect ratio (A) = 5, the collapse timescale at its edges is observed 2–3 times less compared to the central regions, while those with higher aspect ratio collapse much faster at the ends (see Figures 5 and 6 in Pon et al. 2011). Here A is defined as $\frac{L}{R}$, where $2L$ is the length of the filament and R is the radius of it (e.g., Bastien 1983; Toalá et al. 2012; Pon et al. 2012). The faster collapse at the edges of the filament is supported by the high preferential acceleration of the gas, which leads to density enhancement there (see Section 2.2 in Pon et al. (2012)). Interestingly, the western part of the filament is found to have higher accretion rate (i.e., $\sim 60 M_{\odot} \text{ pc}^{-1} \text{ Myr}^{-1}$) compared to the central part (i.e., $\sim 22 M_{\odot} \text{ pc}^{-1} \text{ Myr}^{-1}$; see Section 4.2). The homologous collapse is observed if A is less than 5, while the end-dominated collapse is dominant if $A \geq 5$ (Pon et al. 2011, 2012). Using the ^{13}CO moment-0 map (see Figure 5d), the observed aspect ratio of the Mon R1 filament is estimated to be ~ 11.5 (i.e., for length ~ 14 pc and diameter ~ 1.2 pc). This value is larger than 5, suggesting the faster collapse at its ends.

Observationally, we find embedded *Herschel* high column density regions/fragments and the periodic oscillation in the velocity profile of the filament, tracing the ongoing fragmentation and formation of the precursor of potential gravitationally bound cores. Furthermore, clusters of YSOs, sites IC 446 and IC 447, and massive B-type stars are observed at the ends of the filament. It suggests the intense star formation activities at the filament ends compared to its central part, implying that the local collapse had occurred faster at the filament ends. Altogether, our observational results are consistent with the “end dominated collapse” model of star formation in Mon R1 filament. The observational examples of end dominated fragments/clumps or end dominated collapse scenario are a few in the literature (such as, NGC 6334 (Zernickel et al. 2013); IRDC 18223 (Beuther et al. 2015); Musca cloud (Hacar et al. 2016; Kainulainen et al. 2016); S242 (Dewangan et al. 2017c, 2019); G341.244–00.265 (Yu et al. 2019)). Out of these, the filament in S242 shows the evolved phase of filamentary fragmentation as its one end hosts the S242 HII region, which might have formed by the process of “end dominated collapse”. Rest of the mentioned filaments are caught in their very early phases of fragmentation as they show dense clumps along their major axis. At least one of the ends of a few filaments show higher velocity gradients compared to central region (e.g., $0.5 \text{ km s}^{-1} \text{ pc}^{-1}$ toward the southern end of Musca cloud (Hacar et al. 2016; Kainulainen et al. 2016); $1 \text{ km s}^{-1} \text{ pc}^{-1}$ toward both the ends of S242 (Dewangan et al. 2017c, 2019); $0.6\text{--}0.8 \text{ km s}^{-1} \text{ pc}^{-1}$ toward one end of G341.244–00.265 (Yu et al. 2019)). In contradiction, the filament in NGC 6334 displays the velocity gradient from the ends toward the centre (Zernickel et al. 2013), and IRDC 18223 filament shows a transverse velocity gradient at one of its ends instead of showing velocity

gradient along the major axis.

In comparison to the listed filaments, Mon R1 filament can be treated as the best example of a more evolved stage of the filamentary fragmentation, which reveals end dominated collapse thus forming the known massive star-forming sites at the ends. Our observational analysis shows the clear linear velocity gradient along the central part of the filament ($\sim 0.4 \text{ km s}^{-1} \text{ pc}^{-1}$), and relatively higher velocity gradients ($\sim 0.6 \text{ km s}^{-1} \text{ pc}^{-1}$) at the ends, which are probably associated with star-forming regions.

5. SUMMARY AND CONCLUSIONS

This paper aims to understand the physical processes governing the star formation activities in Mon R1 filament. In this context, a multi-wavelength observational approach has been employed in Mon R1 complex. Our major observational results are pointed below:

- The optical and infrared images show the existence of a filament (length ~ 14 pc, mass $\sim 1465 M_{\odot}$) in Mon R1, which is the most prominent feature in the *Herschel* column density map.
- Using the ^{12}CO and ^{13}CO line data, two molecular clouds at $[-5, 1]$ and $[2, 10] \text{ km s}^{-1}$ are traced toward our selected target area. The molecular gas associated with the filament is studied in a velocity range of $[-5, 1] \text{ km s}^{-1}$, which is found to be isolated from another diffuse cloud at $[2, 10] \text{ km s}^{-1}$. The analysis of molecular gas has enabled us to depict the exact boundaries of the filamentary cloud.
- The filament is found to contain two previously known sites IC 446 and IC 447 at its opposite ends. Several massive B-type stars are identified toward the site IC 447, while a massive YSO (i.e., VY Mon) is observed toward the site IC 446.
- The extended temperature features (at $T_d \sim 15\text{--}21$ K), PDRs, and outflow activity are observed toward both the ends of the filament, suggesting the ongoing star formation activity.
- The study of the distribution of selected YSOs reveals clustering of YSOs mainly toward the ends of the filament (i.e., IC 446 and IC 447). Higher surface density of YSOs (i.e., $4\text{--}125 \text{ YSOs pc}^{-2}$) is traced toward IC 446, while in the direction of IC 447, the surface density is found to be $4\text{--}12 \text{ YSOs pc}^{-2}$. It indicates the intense star formation activities toward IC 446 compared to IC 447.
- Using the *Herschel* column density map, the total estimated mass of the filament (length ~ 14 pc) is $\sim 1465 M_{\odot}$, which yields the observed line mass ($M_{l,obs}$) to be $\sim 105 M_{\odot} \text{ pc}^{-1}$. The critical line mass of the filament ($M_{l,cri}$) is computed to be $\sim 24\text{--}32 M_{\odot} \text{ pc}^{-1}$ for a temperature range of $\sim 15\text{--}20$ K. It implies that $M_{l,obs}$ is $\sim 3\text{--}4$ times more than $M_{l,cri}$, suggesting the existence of a thermally *supercritical* filament in Mon R1.
- The western part of the filament takes about 0.4 Myr to grow its line mass by its critical value with an average accretion rate of $\sim 60 M_{\odot} \text{ pc}^{-1} \text{ Myr}^{-1}$. In the case of the central part of the filament, this critical timescale and the accretion rate are estimated to be ~ 1.1 Myr and $\sim 22 M_{\odot} \text{ pc}^{-1} \text{ Myr}^{-1}$, respectively.
- The velocity and linewidth profiles of the filament show an oscillatory pattern with a periodicity of 3–4 pc along the direction of its major axis. The velocity

gradient along the central part of the filament is found to be ($\sim 0.4 \text{ km s}^{-1} \text{ pc}^{-1}$), however the relatively higher velocity gradients ($\sim 0.6 \text{ km s}^{-1} \text{ pc}^{-1}$) are observed at both the ends of the filament.

- The aspect ratio (A) of the filament is found to be greater than 5, suggesting the end dominated collapse mode is dominated over the homologous collapse mode.

Taken together, all the observational outcomes, the fragments distributed toward both the ends of the filament are found to undergo a faster collapse compared to its central part, showing the presence of massive star-forming regions at its opposite ends. Overall, the elongated filament in Mon R1 is a promising candidate favouring the “end-dominated collapse” model of star formation as discussed by Pon et al. (2011, 2012).

We thank the anonymous reviewer for several useful comments and suggestions. The research work at Physical Research Laboratory is funded by the Department of Space, Government of India. This work is based on data obtained as part of the UKIRT Infrared Deep Sky Survey. This publication makes use of data products from the Two Micron All Sky Survey, which is a joint project of the University of Massachusetts and the Infrared Processing and Analysis Center/California Institute of Technology, funded by NASA and NSF. This work is based [in part] on observations made with the *Spitzer* Space Telescope, which is operated by the Jet Propulsion Laboratory, California Institute of Technology under a contract with NASA. This publication makes use of data from FUGIN, FOREST Unbiased Galactic plane Imaging survey with the Nobeyama 45-m telescope, a legacy project in the Nobeyama 45-m radio telescope. LEP acknowledges support of the Russian Science Foundation (project 17-12-01256). DKO acknowledges the support of the Department of Atomic Energy, Government of India, under project No. 12-R&D-TFR-5.02-0200.

REFERENCES

- André, P., Men'shchikov, A., Bontemps, S., et al. 2010, *A&A*, 518, L102
- André, P., Di Francesco, J., Ward-Thompson, D., et al. 2014, in *Protostars and Planets VI*, ed. H. Beuther et al. (Tucson, AZ: Univ. Arizona Press), 27
- Bally, J., Lanber, W. D., Stark, A. A., et al. 1987, *ApJ*, 312, L45
- Banerjee R., Pudritz R. E., 2008, in Beuther H., Linz H., Henning T., eds, *ASP Conf. Ser. Vol. 387, Massive Star Formation: Observations Con- front Theory*. Astron. Soc. Pac., San Francisco, p. 216
- Bastien, P. 1983, *A&A*, 119, 109
- Bastien, P., Arcoragi, Jean-Pierre, Benz, W., et al. 1991, *ApJ*, 378, 255
- Baug, T., Ojha, D. K., Dewangan, L. K., et al. 2015, *MNRAS*, 454, 4335
- Benjamin, R. A., Churchwell, E., Babler, B. L., et al. 2003, *PASP*, 115, 953
- Beuther, H., Ragan, S. E., Johnston, K., et al. 2015, *A&A*, 584A, 67
- Bressert, E., Bastian, N., Gutermuth, R., et al. 2010, *MNRAS*, 409, 54
- Busquet, G., Zhang, Q., Palau, A., et al. 2013, *ApJL*, 764, L26
- Cannon, A. J., & Pickering, E. C. 1993, *yCat*, 3135, 0
- Casertano, S., & Hut P. 1985, *ApJ*, 298, 80
- Casey, S. C., & Harper, D. A. 1990, *ApJ*, 362, 663
- Clarke, S. D., & Whitworth, A. P. 2015, *MNRAS*, 449, 1819
- Clarke, S. D., Whitworth, A. P., & Hubber, D. A. 2016, *MNRAS*, 458, 319
- Condon, J. J., Cotton, W. D., Greisen, E. W., et al. 1998, *AJ*, 115, 1693
- Contreras, Y., Rathborne, J., & Garay, G. 2013, *MNRAS*, 433, 251
- Contreras, Y., Garay, G., Rathborne, J. M., & Sanhueza, P. 2016, *MNRAS*, 456, 2041
- Dewangan, L. K., Luna, A., Ojha, D. K., et al. 2015, *ApJ*, 811, 79
- Dewangan, L. K., Ojha, D. K., Luna, A., et al. 2016a, *ApJ*, 819, 66
- Dewangan, L. K., Ojha, D. K., Zinchenko, I., et al. 2016b, *ApJ*, 833, 246
- Dewangan, L. K., Ojha, D. K., Zinchenko, I., Janardhan, P., & Luna, A. 2017a, *ApJ*, 834, 22
- Dewangan, L. K., Ojha, D. K., & Baug, T. 2017b, *ApJ*, 844, 15
- Dewangan, L. K., Baug, T., Ojha, D. K., Janardhan, P., Devaraj, R., & Luna, A. 2017c, *ApJ*, 845, 34
- Dewangan, L. K., Devaraj, R., Baug, T., & Ojha, D. K. 2017d, *ApJ*, 848, 51
- Dewangan, L. K., Ojha, D. K., & Zinchenko, I. 2017e, *ApJ*, 851, 140
- Dewangan, L. K., Baug, T., Ojha, D. K., et al. 2018, *ApJ*, 864, 54
- Dewangan, L. K., Pirogov, L. E., & Ryabukhina, O. L., 2019, *ApJ*, 877, 1
- Flaherty, K. M., Pipher, J. L., Megeath, S. T., Winston, E. M., et al. 2007, *ApJ*, 663, 1069
- Goodman, A. A., Alves, J., Beaumont, C. N., et al. 2014, *ApJ*, 797, 53
- Gutermuth, R. A., Megeath, S. T., Myers, P. C., et al. 2009, *ApJS*, 184, 18
- Hacar, A. & Tafalla, M. 2011, *A&A*, 533, A34
- Hacar, A., Kainulainen, J., Tafalla, M., et al. 2016, *A&A*, 587A, 97
- Heitsch, F., Hartmann, L. W., Slyz, A. D., Devriendt, J. E.G., & Burkert, A. 2008, *ApJ*, 674, 316
- Herbst, W., Miller, D. P., Warner, J. W., et al. 1982, *AJ*, 87, 98
- Inutsuka, S. & Miyama, S. M. 1992, *ApJ*, 388, 392
- Inutsuka, S. & Miyama, S. M. 1997, *ApJ*, 480, 681
- Jackson, J. M., Finn, S. C., Chambers, E. T., et al. 2010, *ApJ*, 719L, 185
- Kainulainen, J., Hacar, A., Alves, J., et al. 2016, *A&A*, 586, 27
- Kutner, M. L., Dickman, R. L., Tucker, K. D. 1979, *ApJ*, 232, 724
- Lawrence, A., Warren, S. J., Almaini, O., et al. 2007, *MNRAS*, 379, 1599
- Lu, X., Zhang, Q., Liu, H. B., et al. 2018, *ApJ*, 855, 9
- Marsh, K. A., Whitworth, A. P., & Lomax, O. 2015, *MNRAS*, 454, 4282
- Marsh, K. A., Whitworth, A. P., Lomax, O., et al. 2017, *MNRAS*, 471, 2730
- McLean, B. J., Greene, G. R., Lattanzi, M. G., & Pirenne, B. 2000, *ASPC*, 216, 145
- Molinari, S., Swinyard, B., Bally, J., et al. 2010a, *A&A*, 518, L100
- Molinari, S., Swinyard, B., Bally, J., et al. 2010b, *PASP*, 122, 314
- Montillaud, J., Juvela, M., Vastel, C., et al. 2019, *A&A*, 631, A3
- Mora, A., Mern, B., Solano, E., et al. 2001, *A&A*, 378, 116
- Movsessian, T. A., Magakian, T. Yu., & Dodonov, S. N. 2020, *arXiv*, 200504257
- Myers, P. C. 2009, *ApJ*, 700, 1609
- Nakamura, F., Hanawa, T., & Nakano, T. 1993, *PASJ*, 45, 551
- Nassau, J. J., Stephenson, C. B., & McConnell, D. J. 1965, *Hamburger Sternw. Warner & Swasey Obs.*, C06, 0
- Oliver, R. J., Masheder, M. R. W., & Thaddeus, P. 1996, *A&A*, 315, 578
- Ostriker, J. 1964, *ApJ*, 140, 1056
- Pilbratt, G. L., Riedinger, J. R., Passvogel, T., et al. 2010, *A&A*, 518L, 1
- Planck Collaboration IX. 2014, *A&A*, 571, A9
- Pon, A., Johnstone, D., & Heitsch, F. 2011, *ApJ*, 740, 88
- Pon, A., Toalá, J. A., Johnstone, D., et al. 2012, *ApJ*, 756, 145
- Racine, R. 1968, *AJ*, 73, 233
- Schneider, N., Csengeri, T., Bontemps, S., et al. 2010, *A&A*, 520, A49
- Schneider, N., Csengeri, T., Hennemann, M., et al. 2012, *A&A*, 540, L11

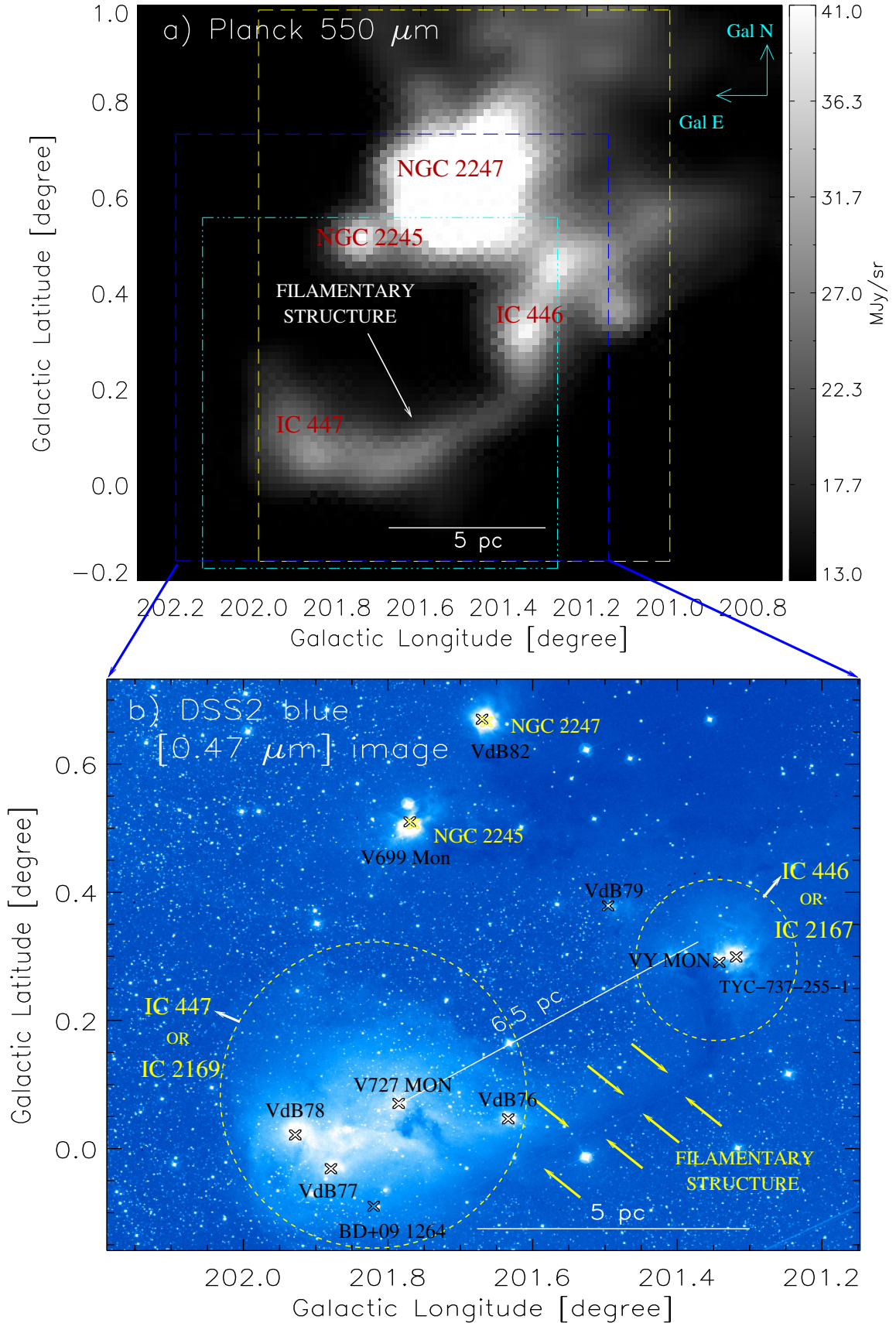


Figure 1. The R-association in Mon R1 complex. a) *Planck* continuum image at 550 μm . A filamentary structure seen in the image is marked by an arrow. A dashed box (in blue) shows the area presented in Figure 1b. A dotted-dashed box (in cyan) and a rectangular box (in yellow) represent the areas shown in Figures 2 and 5, respectively. b) A zoomed-in optical image at DSS2 0.47 μm of Mon R1 (see a dashed blue box in Figure 1a). The extent of known reflection nebulae IC 446 and IC 447 are shown by dashed circles. A dark-filament connecting these nebulae is highlighted by yellow arrows. The positions of previously known B-type stars and reflection nebulae (i.e., NGC 2245 and NGC 2247) are indicated and labeled by black and yellow color cross symbols, respectively (see Table 1). A scale bar representing 5 pc (at d \sim 760 pc) is shown in each panel.

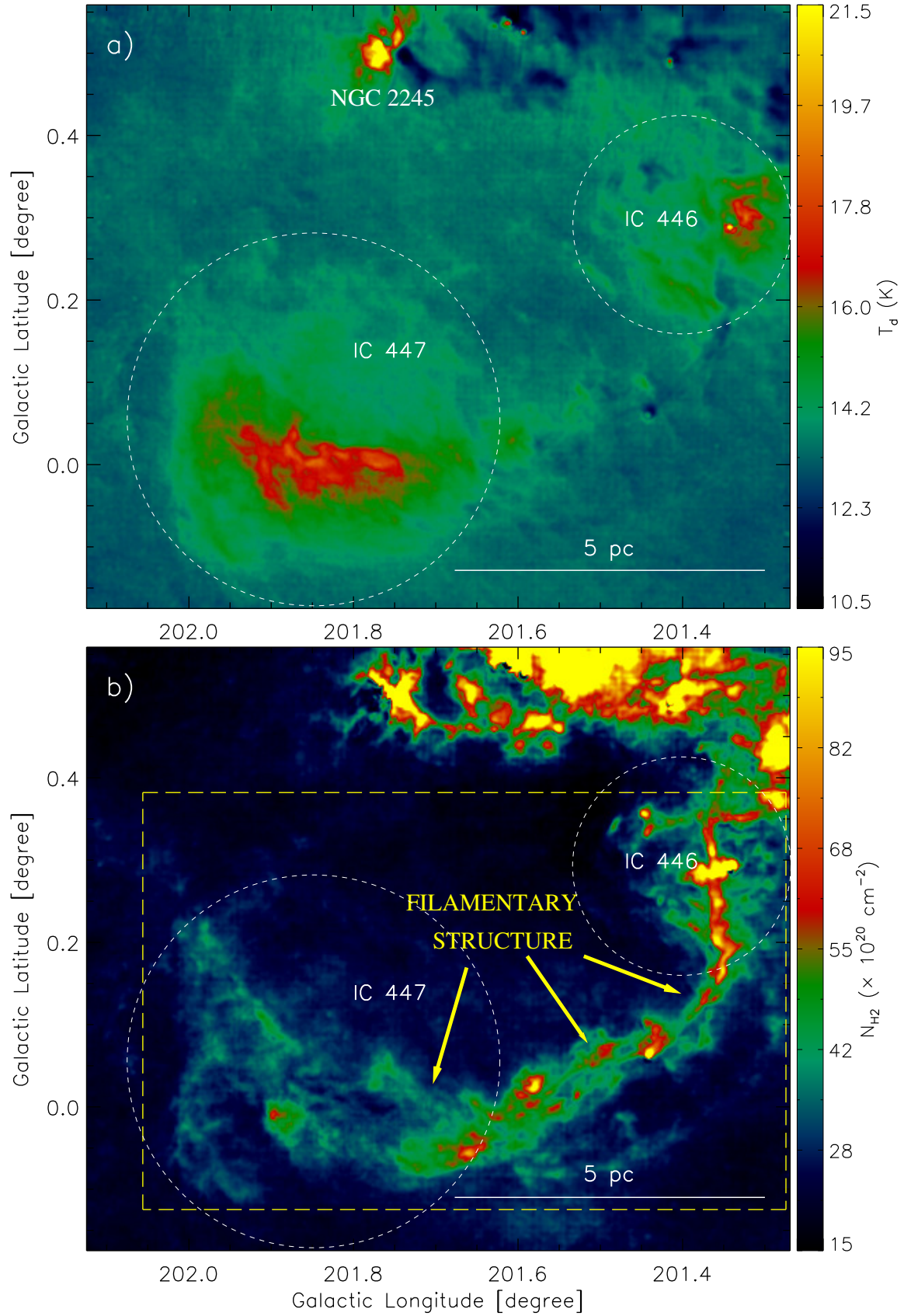


Figure 2. a) *Herschel* temperature map of the region containing the filament (see a dotted-dashed cyan box in Figure 1a). b) *Herschel* column density map. The identification of *Herschel* dust clumps is carried out in the area shown by a dashed yellow box (see Figure 3). In each panel, broken circles indicate the extent of IC 446 and IC 447. A scale bar corresponding to 5 pc is shown in both panels.

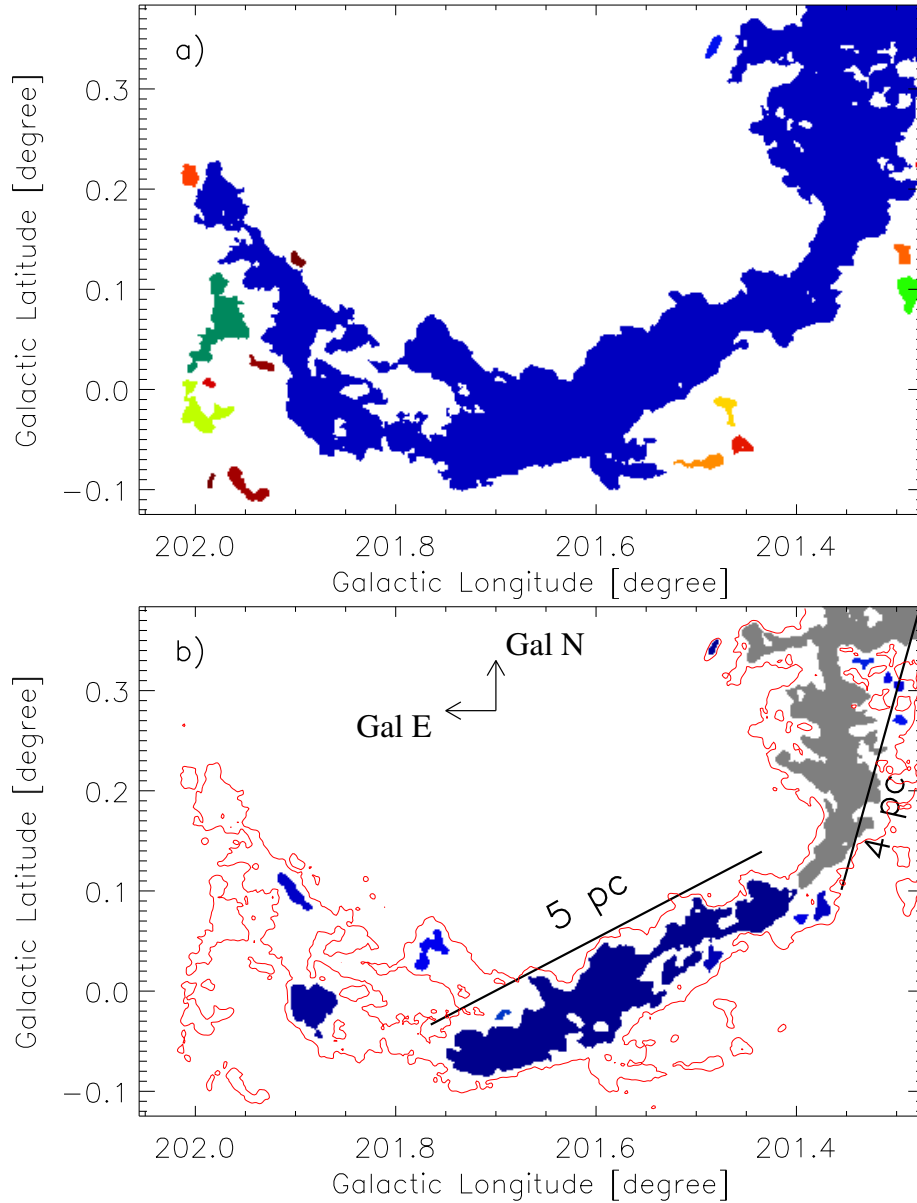


Figure 3. a) An elongated filament is depicted in the column density map with the $N(\text{H}_2)$ contour level of $3.2 \times 10^{21} \text{ cm}^{-2}$. b) Two sub-filaments (central in blue, and western in gray) are identified in the direction of the elongated filament using the $N(\text{H}_2)$ contour level of $4.1 \times 10^{21} \text{ cm}^{-2}$. The projected length of each sub-filament is indicated by a scale bar. The $N(\text{H}_2)$ contour (in red) is also overplotted to show the elongated filament as shown in Figure 3a.

Skrutskie, M. F., Cutri, R. M., Stiening, R., et al. 2006, *AJ*, 131, 1163
 Stahler, S. W., & Palla, F. 2005, Wiley-VCH, *The Formation of Stars*, 865
 Tielens, A. G. G. M. 2008, *ARA&A*, 46, 289
 Toalá, J. A., Vázquez-Semadeni, & E., Gómez, G. C. 2012, *ApJ*, 744, 190
 Tobin, J. J., Hartmann, L., Looney, L. W., Chiang, & Hsin-Fang. 2010, *ApJ*, 712, 1010
 Umemoto, T.; Minamidani, T.; Kuno, N., et al. 2017, *PASJ*, 69, 78

van den Bergh, S. 1966, *AJ*, 71, 990
 Whitney, B., Benjamin, R., Meade, M., et al. 2011, *Bulletin of the American Astronomical Society*, Vol. 43
 Williams, de Geus, & Blitz 1994, *ApJ*, 428, 693
 Williams, G. M., Peretto, N., Avison, A., et al. 2018, *A&A*, 613A, 11
 Wright, E. L., Eisenhardt, P. R. M., Mainzer, A. K., et al. 2010, *AJ*, 140, 1868
 Yu, Nai-Ping, Xu, Jing-Long, & Wang, Jun-Jie 2019, *A&A*, 622A, 155
 Zernicke, A., Schilke, P., & Smith, R. J. 2013, *A&A*, 554L, 2

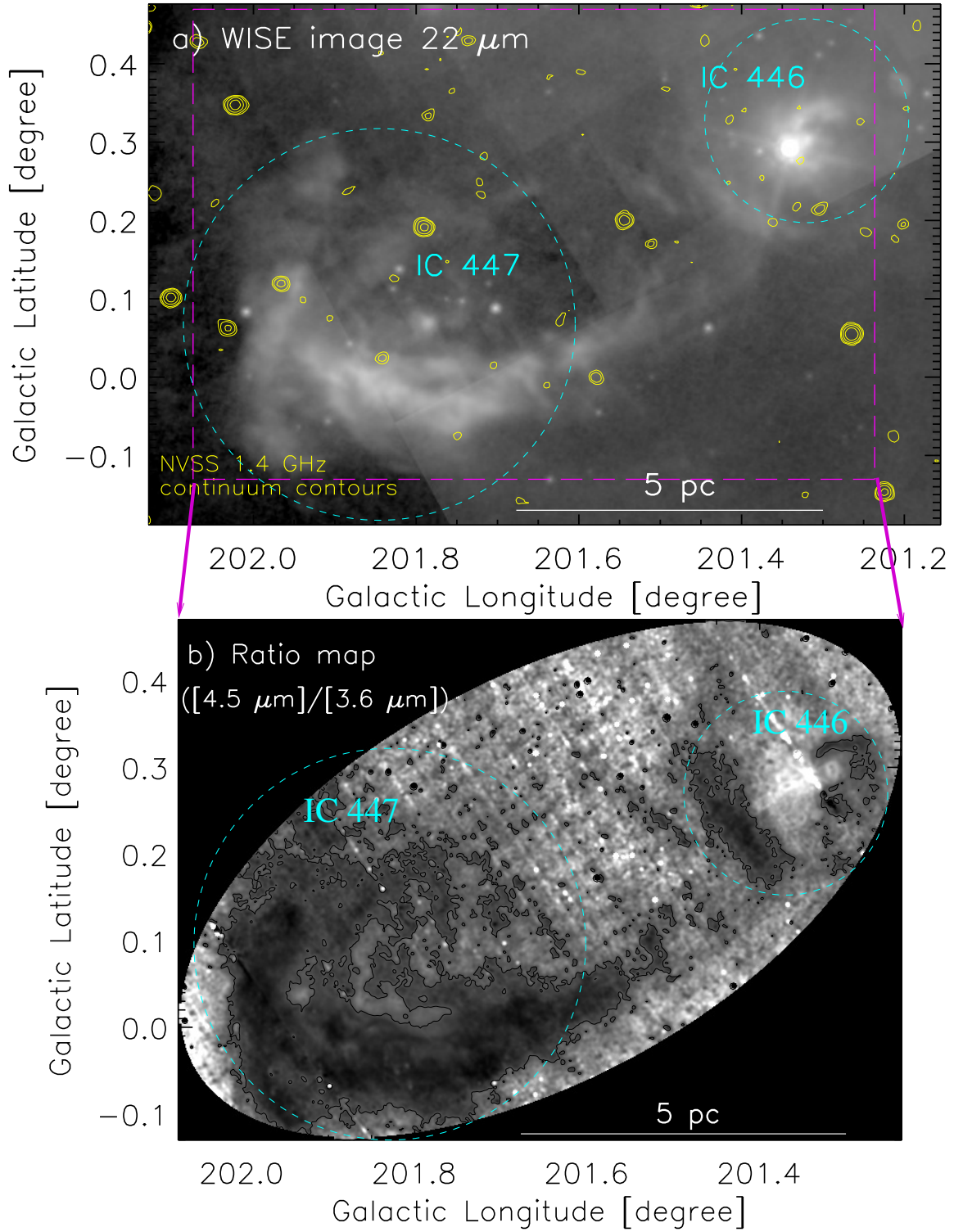


Figure 4. a) Overlay of the NVSS radio 1.4 GHz continuum emission contours on the MIR image at *WISE* $22\ \mu\text{m}$ toward the filament. The NVSS contours are shown with the levels $(3, 5, 10, 20) \times 1\sigma$, where $1\sigma = 0.45\ \text{mJy beam}^{-1}$. A dashed box (in magenta) encompasses the area shown in Figure 4b. b) *Spitzer* ratio map of $4.5\ \mu\text{m}/3.6\ \mu\text{m}$ emission. Broken circles show the extent of IC 446 and IC 447 in each panel. The ratio map is smoothed using a Gaussian function with radius of three pixels. A scale bar corresponding to 5 pc is displayed in both panels.

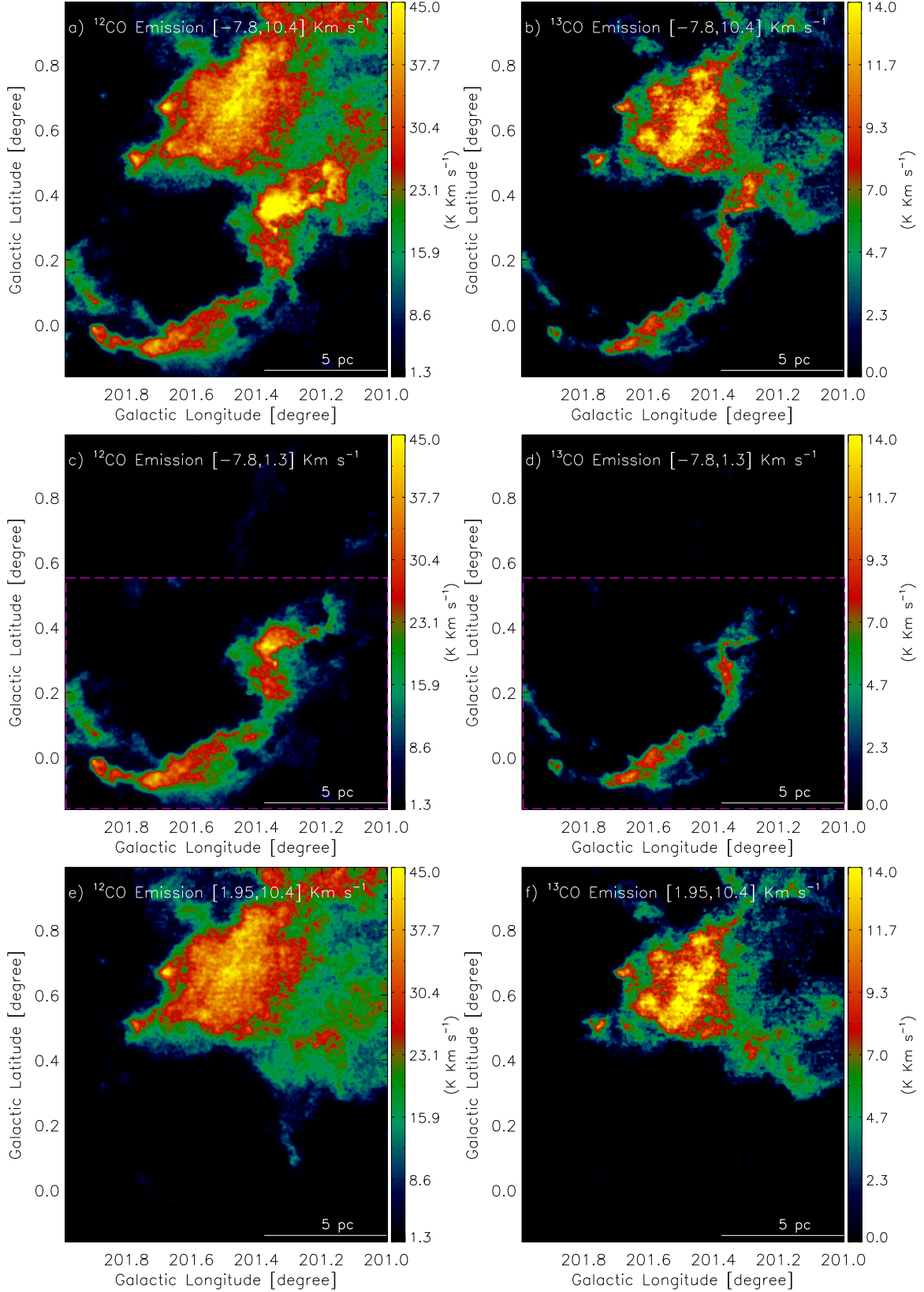


Figure 5. Left column: “a”, “c”, “e” FUGIN $^{12}\text{CO}(1-0)$ map of intensity (moment-0) in the direction of Mon R1. Right column: “b”, “d”, “f” FUGIN $^{13}\text{CO}(1-0)$ map of intensity (moment-0) in the direction of Mon R1. In panels “a” and “b”, the molecular emission is integrated over a velocity range of $[-7.8, 10.4] \text{ km s}^{-1}$. In panels “c” and “d”, the molecular emission is integrated over a velocity range of $[-7.8, 1.3] \text{ km s}^{-1}$. In panels “e” and “f”, the molecular emission is integrated over a velocity range of $[1.95, 10.4] \text{ km s}^{-1}$. A scale bar corresponding to 5 pc is shown in each panel. In panels “c” and “d”, the molecular emission is observed mainly toward the filament, which is highlighted by a broken box (in magenta).

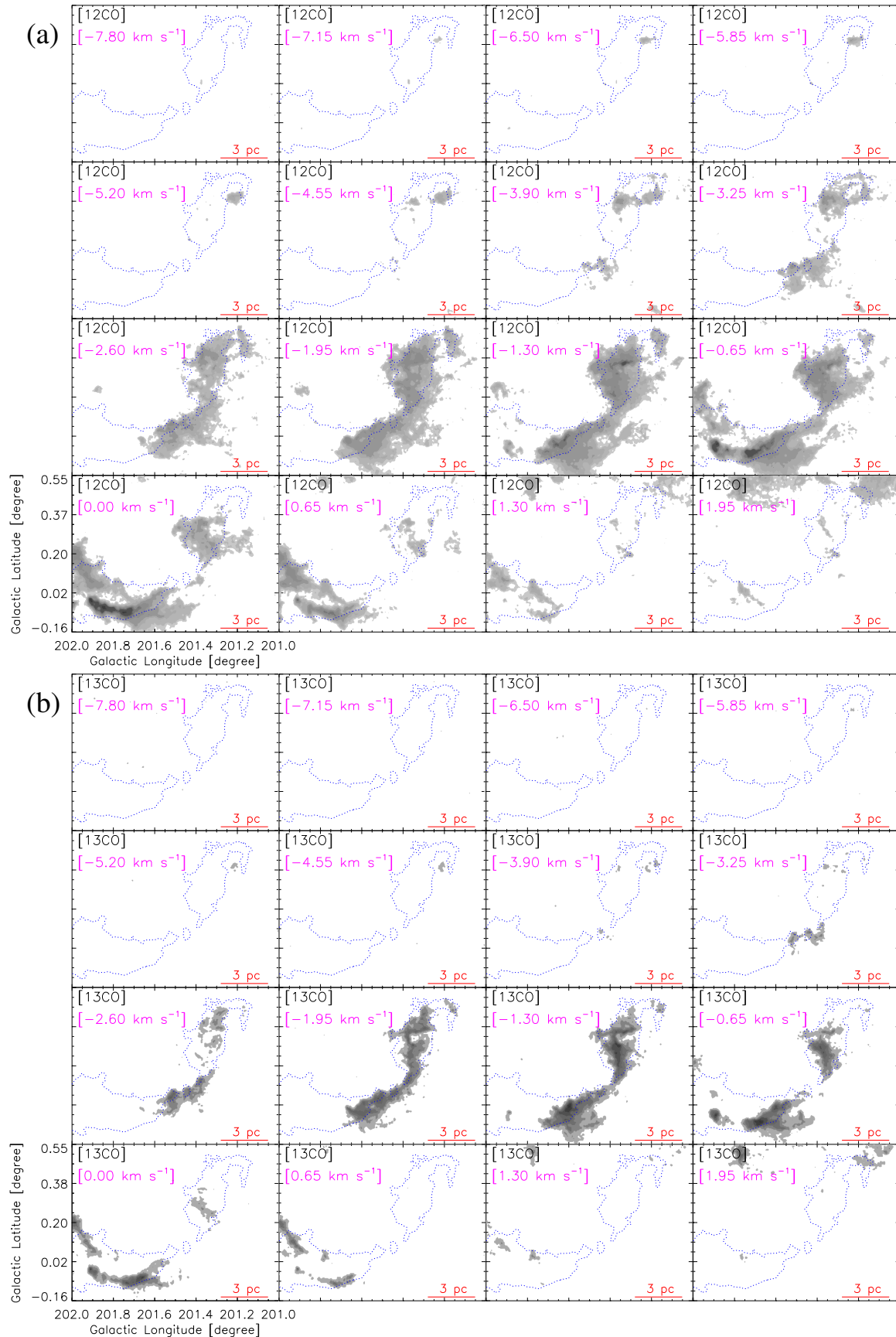


Figure 6. a) Velocity channel maps of ¹²CO(1–0) toward the region marked by a dashed magenta box in Figures 5c and 5d. The contour levels are 1.5, 3, 5, 7, 10, 13, 15, 16, 20, and 23 K km s⁻¹. b) Velocity channel maps of ¹³CO(1–0). The contour values are 0.1, 0.5, 1, 1.5, 2, 3, 4, 5, 6, and 7 K km s⁻¹. The *Herschel* 160 μm continuum emission contour (in blue with a level of 0.02 Jy pixel⁻¹ is overplotted in each panel. In each panel, the velocity information (in km s⁻¹) and a scale bar representing 3 pc are shown.

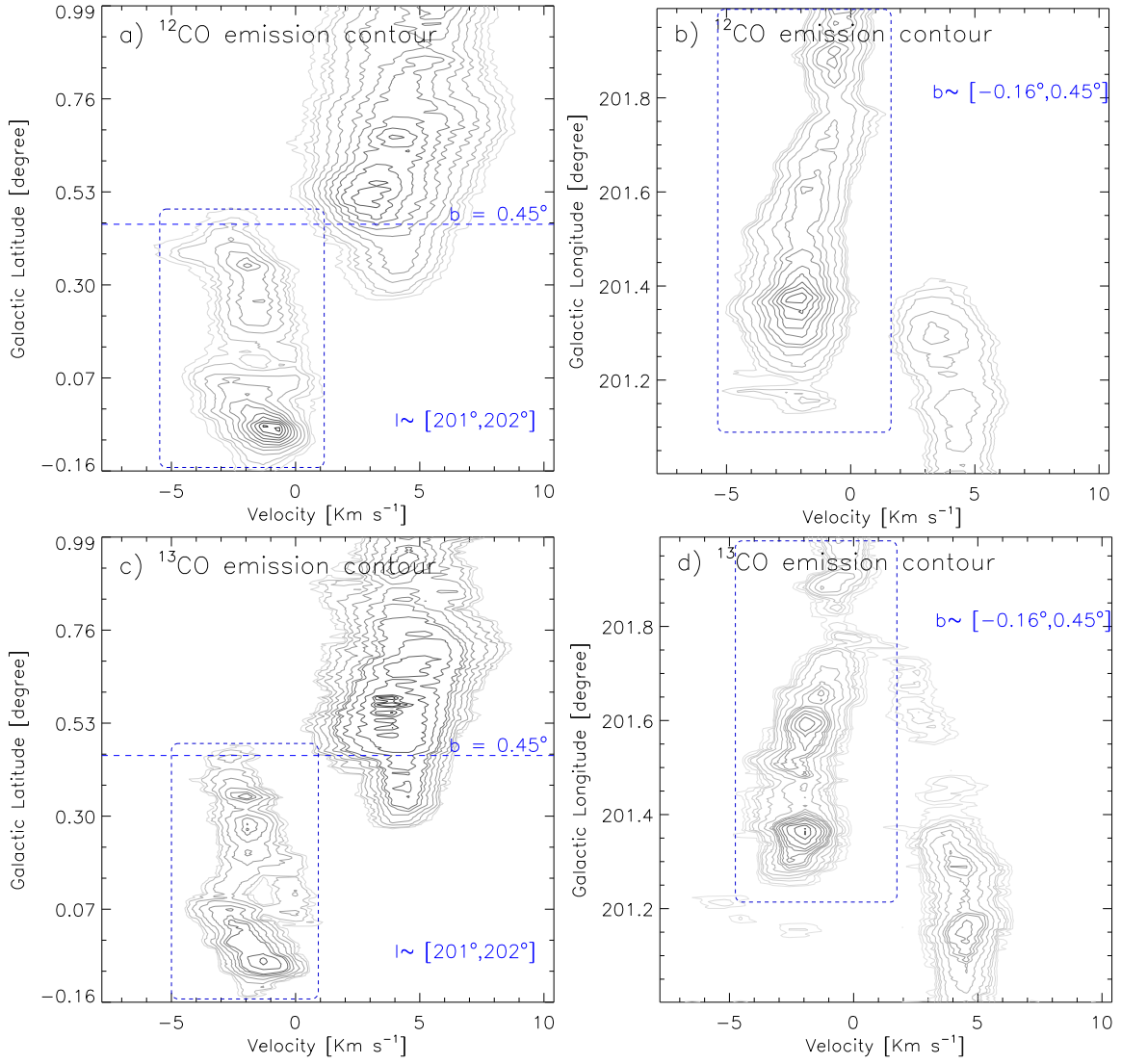


Figure 7. a) Latitude-velocity diagram of ^{12}CO . b) Longitude-velocity diagram of ^{12}CO . c) Latitude-velocity diagram of ^{13}CO . d) Longitude-velocity diagram of ^{12}CO . In the latitude-velocity diagrams (see panels “a” and “c”), the molecular emission is integrated over the longitude range from 201° to 202° (see a broken box in Figures 5c and 5d). In the longitude-velocity diagrams (see panels “b” and “d”), the molecular emission is integrated over the latitude range from -0.16° to 0.45° . In each panel, a dashed rectangular box (in blue) depicts the CO emission toward the filament (see text for more details).

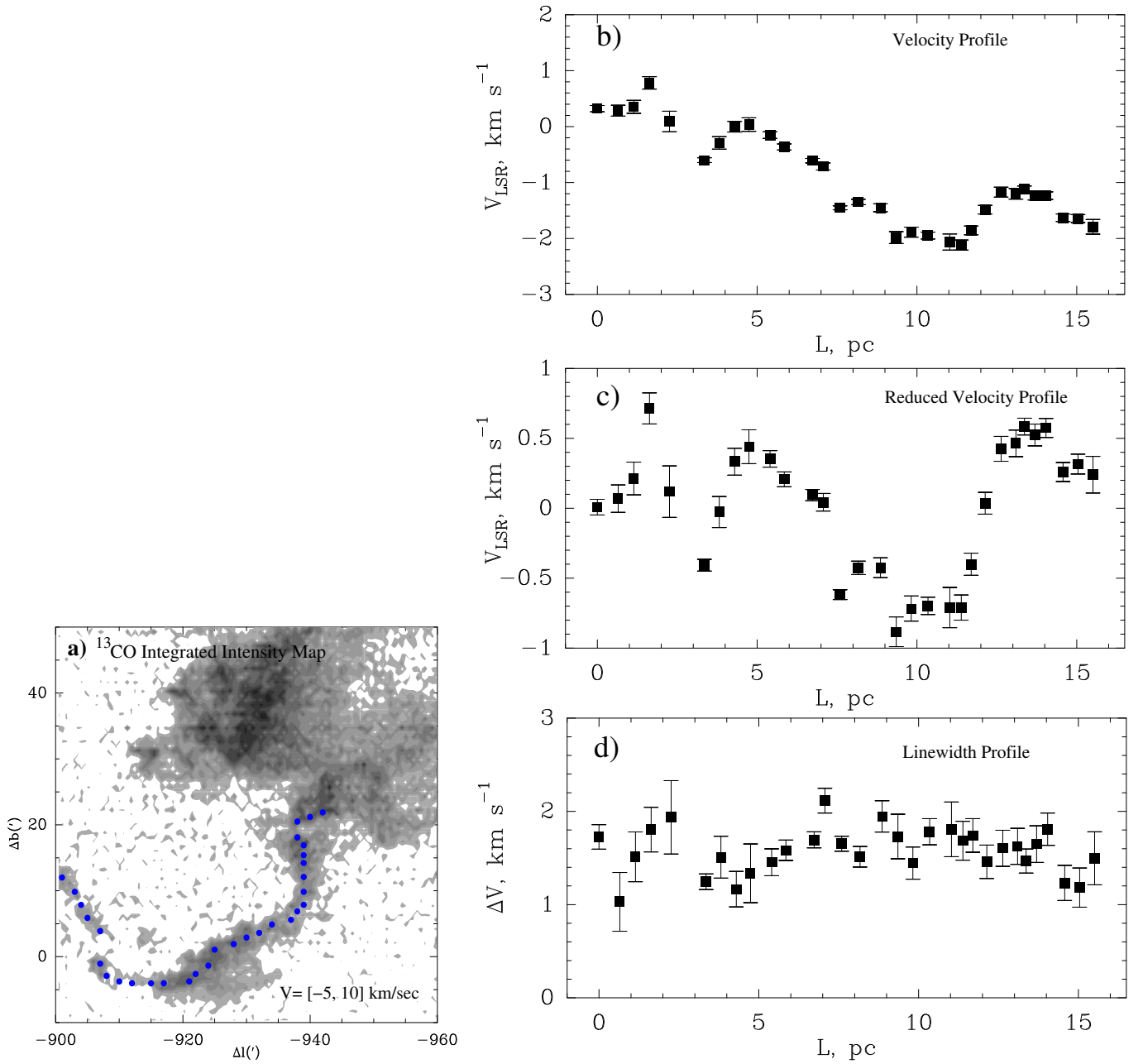


Figure 8. a) FUGIN $^{13}\text{CO}(1-0)$ map of intensity (moment-0) in the direction of Mon R1. The molecular emission is integrated over a velocity range of $[-5, 10]$ km s $^{-1}$. Blue dots are marked toward the filamentary structure, where spectra are extracted. b) Velocity profile along the filament obtained from distinct positions (see blue dots in panel “a”). c) Velocity profile after removing the linear gradient from profile shown in panel “b”. d) Linewidth profile (average linewidth ~ 1.5 km s $^{-1}$). In panels “b”, “c”, and “d”, the x-axis represents the physical length.

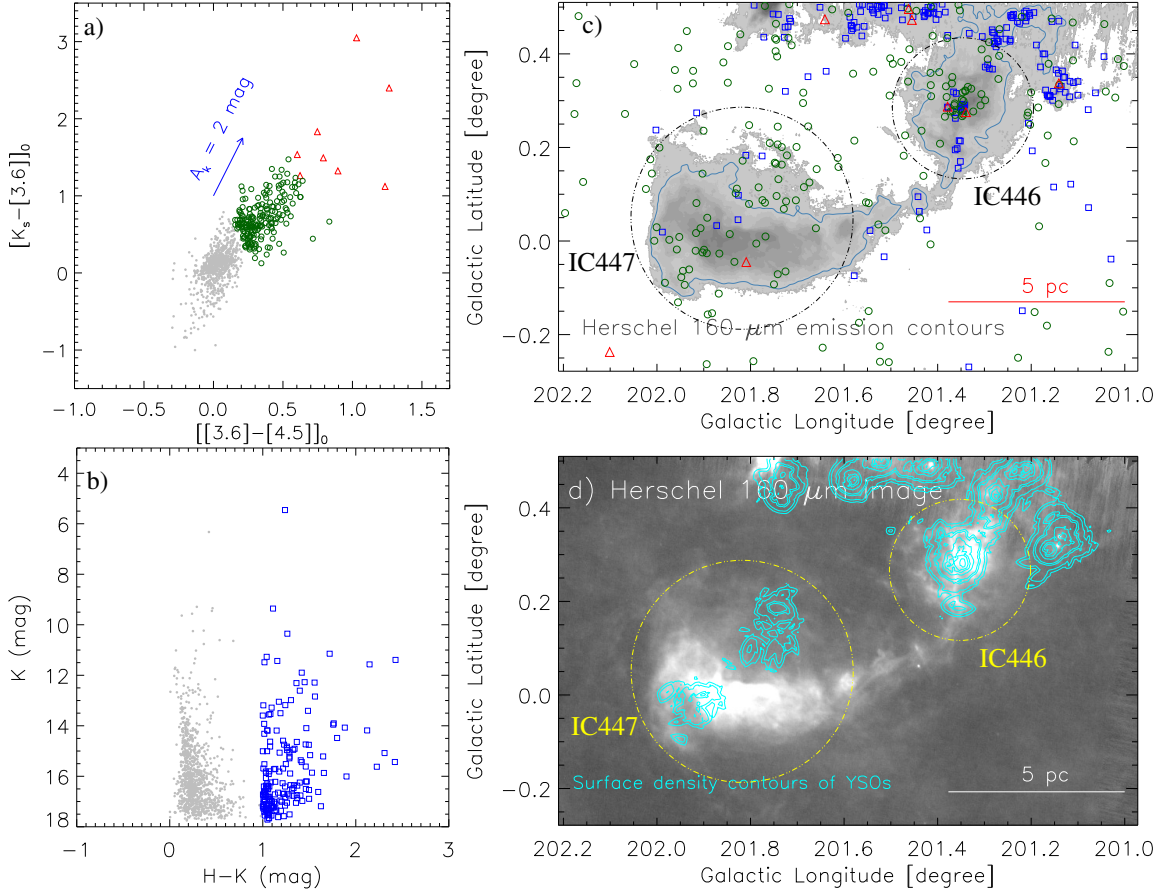


Figure 9. a) Dereddened color-color ($[[3.6] - [4.5]]_0$ vs $[K - [3.6]]_0$) diagram of point-like objects toward Mon R1. Red triangles represent Class I YSOs, while green circles indicate Class II YSOs (see text for more details). Following the extinction law given in Flaherty et al. (2007), an extinction vector ($A_K = 2$ mag) is drawn in the figure. b) Color-magnitude ($H - K$ vs K) diagram of point-like sources. The color excess sources are highlighted by blue squares. c) Overlay of the selected YSOs (from panels “a” and “b”) on the *Herschel* 160 μm gray-scale filled contour map. The contour values are 0.8%, 1.5%, 2%, 2.5%, 3%, 4%, 5%, 7%, 9%, 15%, 30%, 50%, 70%, 90%, 95% of the peak value (i.e., $1.68 \text{ Jy pixel}^{-1}$). A contour (in sky-blue color) with a level of $0.02 \text{ Jy pixel}^{-1}$ is also displayed in the figure. d) Overlay of the surface density contours (in cyan) of YSOs on the *Herschel* continuum map at 160 μm . The surface density contours are presented with the levels of 4, 5, 8, 10, 20, 35, 55, and 125 YSOs pc^{-2} . In panels “c” and “d”, a scale bar corresponding to 5 pc is shown, and big dotted circles represent the extent of IC 446 and IC 447. In panels “a” and “b”, sources with photospheric emission are shown by dots (in grey). Due to a large number of these sources, a small fraction is randomly displayed in panels “a” and “b”.